Observation and prediction of dynamic ground strains, tilts and torsions caused by the M6.0 2004 Parkfield, California, earthquake and aftershocks derived from UPSAR array observations

Paul Spudich

Jon B. Fletcher

both at

U. S. Geological Survey, MS977, Menlo Park, California 94025, USA

spudich@usgs.gov
jfletcher@usgs.gov

v24

for publication in

Bulletin of the Seismological Society of America

submitted: June 15, 2007

revised: January 9, 2008

second revision: February 5, 2008

accepted: February 12, 2008

third revision: March 20, 2008

second acceptance: March 20, 2008

Abstract

The September 28, 2004, Parkfield, California, earthquake (M_w 6.0) and four aftershocks (M_w 4.7 - 5.1) were recorded on 12 accelerograph stations of the UPSAR seismic array, an array of three-component accelerographs occupying an area of about 1 km^2 located 8.8 km from the San Andreas fault. Peak horizontal acceleration and velocity at UPSAR during the mainshock were 0.45 g and 27 cm/s, respectively. We determined both time-varying and peak values of ground dilatations, shear strains, torsions, tilts, torsion rates, and tilt rates by applying a time-dependent geodetic analysis to the observed array displacement time series. Array-derived dilatations agree fairly well with point measurements made on high sample rate recordings of the Parkfield-area dilatometers (Johnston et al., 2006). Torsion Fourier amplitude spectra agree well with ground velocity spectra, as expected for propagating plane waves. A simple predictive relation, using predicted peak velocity from the Boore-Atkinson (2007) ground motion prediction relation scaled by a phase velocity of 1 km/s, predicts observed peak Parkfield and Chi-Chi rotations (Huang, 2003) well. However, rotation rates measured during M_w 5 Ito, Japan, events observed on a gyro sensor (Takeo, 1998) are factors of 5 - 60 greater than predicted by our predictive relation. This discrepancy might be caused by a scale-dependence in rotation, with rotations measured over a short baseline exceeding those measured over long baselines. An alternative hypothesis is that events having significant non-double-couple mechanisms, like the Ito events, radiate much stronger rotations than double-couple events. If this is true, then rotational observations might provide an important source of new information for monitoring seismicity in volcanic areas.

Introduction

During an earthquake the ground not only translates laterally and vertically but also undergoes rotations and strains. These strains and rotations might be interesting for several reasons. First, they might have some effect on the rocking and torsion of buildings and on the distortion of long structures like bridges and pipelines (Trifunac, 1982). Second, measurement of ground strain may enable point-measurement of seismic phase velocity (Mikumo and Aki, 1964). Third, strain observations can be converted to stress to infer the stresses induced on the

crust by the passage of seismic waves (Spudich et al., 1995, henceforth S95). Fourth, these observations might provide additional constraints on the seismic source (Takeo and Ito, 1997). In addition, rotation sensors have recently been developed using inertial MEMS (micro electro-mechanical) gyros (Takeo, 1998), electrochemical systems, and ring lasers (Igel et al., 2005) which will provide a level of accuracy not possible ten years ago and yield important comparisons with translational motions.

The September 28, 2004, 1715 UTC Parkfield, California, earthquake and hundreds of its aftershocks were recorded on 12 accelerograph stations of the UPSAR seismic array (Fletcher et al., 1992, 2006), an array of three-component accelerographs occupying an area of about 1 km^2 (Figure 1) located about 9 km from the closest part of the San Andreas fault that ruptured during the mainshock (Figure 2). In this study we analyze the mainshock recordings and the recordings of the three largest aftershocks, the September 28 (day 272) 1724 UTC M4.7 event, the September 29 (day 273) 1710 UTC M5.1 event, and the September 30 (day 274) 1854 UTC M4.9 event (Figure 2, Table 1). Data from the main shock are available at http://nsmp.wr.usgs.gov/data_sets/20040928_1715.html. Stated magnitudes are M_w calculated from seismic moments obtained from the Northern California Earthquake Data Center, which uses recordings from the Berkeley Digital Seismic Network.

These array data give us the opportunity to calculate dynamic strain and rotation at a site that experienced strong motion close to a large earthquake (peak horizontal acceleration and velocity at UPSAR during the mainshock were 0.45 g and 27 cm/s, respectively). Oliveira and Bolt (1989) introduced an approximate method for deriving rotations from array measurements, which Huang (2003) used to estimate rotations from array recordings 6 km from the 1999 M7.6 Chi-Chi, Taiwan, earthquake. A more complete method for estimating rotations and strains from array data was introduced by S95. In that method (called the "seismogeodetic method" by Bodin et al., 1997) the instantaneous deformation of the array is fit by the best-fitting spatially uniform strain and rigid body rotation. The seismogeodetic method differs from the method of Oliveira and Bolt (1989) because the seismogeodetic method uses a generalized inversion of the data and properly accounts for the data covariances.

UPSAR instrumentation is discussed in detail in Fletcher et al. (1992), and the mainshock recordings are presented and interpreted in Fletcher et al. (2006) and Wang et al. (2006). Briefly, each array station consisted of a three-component accelerometer sampled at 200 Hz and digitized using a 16-bit digitizer. Sampling of a particular component of motion at all array stations was synchronized by phase locking each accelerograph's internal clock to a master clock. Consequently, all three components of motion at all stations were sampled essentially simultaneously. The arrival times of S waves are perturbed by site delays caused by differences of seismic velocity under each station. Fletcher et al. (2006) removed these delays from the seismograms. In the following analysis these delays were not removed.

Method

In this paper we apply the seismogeodetic method to the mainshock and aftershock recordings to derive the best fitting uniform strains and rotations as functions of time during the shaking. Specifically, we calculate torsion (rotation around a vertical axis) and torsion rate, tilt (rotation around a horizontal axis) and tilt rate, shear strain, dilatation, horizontal shear strain (shear caused by horizontal deformations), and horizontal dilatation (uniform dilatation caused by horizontal deformations). These quantities and their derivations are given explicitly in Appendix A. We calculate strain in the horizontal plane because building foundations are typically wider than their depth of embedment and are thus more sensitive to horizontal strains. We define tilt to be non-negative, and the axis about which tilt occurs changes with time during the motion (i.e. the local uphill direction rotates during the shaking).

In the seismogeodetic method strains and rotations are determined from ground displacements, which themselves are determined from the doubly-integrated, on-scale acceleration traces. The calculated displacements depend on the steps used in integrating, filtering, and baseline removal. Our process was the following. The original accelerograms were triggered, with only 2 s of pre-event memory. We typically added about 20 1-s duration segments of synthetic noise to the front of the record. The noise had the same mean as the original accelerogram and the same amplitude as the pre-P ground motions. We then demeaned the padded accelerations and windowed the time series to get a trace with about a 100 s

duration. We low-pass filtered each accelerogram at frequency $f_{\max}$, derived below, with an acausal Butterworth filter (six-pole causal, applied forward and backward), and we high-passed with a causal two-pole Butterworth at 10 s period (all events except the M4.7 event 2721724 for which a high-pass corner of 5 s was used). We integrated to velocity, removed the mean of the first 5 s of record from each velocity time series, high-passed again, and cosine tapered the first and last 5% of the filtered velocity time series. We then integrated to displacement and high-pass filtered again. This method was used because it did not have to be modified for each record, and it provided displacement traces with a specified bandwidth. We attempted to integrate traces without high-pass filtering so that near-field offsets in displacements could be recovered, but this procedure entailed changing baseline and filtering steps for each record and was consequently abandoned.

The explicit assumption of the seismogeodetic method is that the strain tensor is spatially uniform over the extent of the array. To guarantee this, we low-pass filter the ground motion data to remove signals with seismic wavelength λ, measured along the Earth's surface, shorter than 4*h*, where *h* is the horizontal extent of the array. The factor of four is derived as follows. From Figure 3 using the small angle approximation it is easy to show that the fractional error in approximating the true slope angle ϕ_t by the slope angle ϕ_c of the chord is

$$e = \frac{\phi_t - \phi_c}{\phi_t} \cong 1 - \frac{\sin(\pi h/\lambda)}{(\pi h/\lambda)}.$$

In this work we have chosen to allow a maximum error *e* of 0.1, which then implies we must require $h < \lambda/4$. Seismic wavelength $\lambda = c/f$, where *f* is frequency and *c* is phase velocity along the Earth's surface. Fletcher et al. (2006, Figure 8) measured $c \geq 2$ km/s at the array for sources in the mainshock and aftershock source areas. Combining these relations tells us that the maximum usable frequency corresponding to $h < \lambda/4$ is $f_{\max} = c/4h$. To apply the seismogeodetic method, we can use subsets of array stations chosen to minimize *h* and maximize $f_{\max}$ in the combinations shown in Table 2.

Based on Table 2, in practice we only apply the seismogeodetic method to the following subsets of array stations: (1, 2, 3), (8, 9, 11), and (5, 6, 7, 8, 9, 11, 12) (Figure 1). (In the following we abbreviate these arrays as 1-3, 8-11, and 5-12, with the latter two implicitly excluding station 10.) Because we want the analysis to have the largest bandwidth possible, we do not use the whole array owing to its low $f_{\max}$ of 0.55 Hz. We do not use the array (5, 6, 7) because the stations are so close together that small errors in the integration of the accelerations to displacements cause large errors in the inferred rotations. A drawback of using three-station arrays like 8-11 is that the seismogeodetic inversion becomes even-determined, with six observations and six unknowns. Consequently, we apply the seismogeodetic inversion to the following combinations of arrays and maximum frequencies. First we calculate strains and rotations in the band up to 1.4 Hz for all events for arrays 1-3, 8-11, and 5-12. Comparison of these results allows us to investigate the accuracy of the three-station results compared to the seven-station results. Then we apply the inversion to 1-3 and 8-11 up to 3.6 Hz for all events, which allows us to investigate strain and rotation in a larger bandwidth. Finally, we estimate peak strains and rotations that are not band-limited by applying correction factors to the measured band-limited observations.

Calculated strains and rotations

Figure 4 shows the strains and rotations calculated from the mainshock displacements on the seven-station array 5-12 in the band 0.1 - 1.4 Hz. the latter being the maximum frequency satisfying the quarter-wavelength criterion for array 5-12 (Table 2). Relating the rows of Figure 4 to quantities in Appendix A, row 1 (solid line) is s^h, the maximum shear strain in the horizontal plane, and the dashed line is total dilatation *d*. The second row is torsion ω_3, and the third row is torsion rate $\dot{\omega}_3$. The fourth row is tilt $\sqrt{\omega_1^2 + \omega_2^2}$, which is non-negative as explained in Appendix A. The fifth row is the time derivative of tilt, the peaks of which are probably biased slightly low because tilt is rectified. Standard deviations, calculated as in the Appendix, are noted. The seventh row is the station 5 north component of velocity. The sixth row is the misfit ratio of S95 Appendix A, which we briefly explain here. At each time step a

best-fitting rigid body rotation and uniform strain are fit to the observed displacements. The misfit is the sum of the lengths of the vector differences between the observed and fitted displacement vectors. The misfit ratio is the ratio of the misfit to the sum of the lengths of all the observed displacement vectors. S95 show that the misfit ratio for uncorrelated Gaussian noise seismograms is approximately unity. We repeated the seismogeodetic analysis for all events on arrays 1-3, 8-11, and 5-12 in the band 0.1 - 1.4 Hz, and for all events on arrays 1-3 and 8-11 in the 0.1 - 3.6 Hz band. Figures 5 and 6 show the mainshock analysis on array 1-3 in the 0.1-1.4 and 0.1-3.6 Hz bands, respectively, and Figure 7 shows the smallest aftershock, the M4.7 2721724 event analyzed on array 8-11 in the 0.1-3.6 Hz band. Table 3 is a summary of bandlimited peak values from all analyses.

As the results in Figure 4 for the mainshock recorded on array 5-12 are probably the most well-determined, we concentrate on them here. We observe a time-variation in the quality of the inversion that might indicate changes in the dominant seismic wavelengths during shaking. The initial P wave arrives at about 21 s, the hypocentral S wave arrives at about 23 s, and the last direct S wave identified by Fletcher et al. (2006) arrives at 30 s, so that all the energy arriving after 30 s might be coda. (The slip model of Liu et al., 2006, has a late source to the northwest not identified by Fletcher et al., and this source might contribute energy after 30 s, although Liu's synthetics for station PHOB, near UPSAR, do not show such a late pulse.) This coda might consist of scattered surface waves; Fletcher et al. (2006) did not detect direct surface waves from the main shock source. The quality of the seismogeodetic fit is shown by the misfit ratio. Before the P wave onset at about 20 s, the misfit ratio is about unity, which is expected for random noise. Periodicity in the pre-P misfit is caused by periodicity in our padded artificial noise. During the P wave the misfit ratio is low, about 0.3, and it rises to about 0.55 during the S wave portion of the record (24 - 30 s), and falls to an average of about 0.35 during the coda from 30 s all the way to a surprising 100 s, indicating that even at 100 s the ground motions cannot be modeled by independent random time series. We speculate that this general variation might be caused by a variation in the dominant seismic wavelength. P waves have higher horizontal phase velocities and propagation velocities than S waves, causing long seismic wavelengths, and dominant frequencies of motion during the coda are lower than during the S wave, also causing long wavelengths. These characteristics could influence the misfit ratio in two ways, first, longer

seismic wavelengths satisfying the spatial uniformity assumption of the seismogeodetic method better, and second, site effects at adjacent stations might be more correlated for longer wavelength waves. We tend to favor the second explanation because we have low pass filtered the data to exclude wavelengths not satisfying the spatial uniformity criterion.

Comparison of the mainshock strains and rotations from subarray 5-12 (Figure 4) with those inferred from subarray 1-3 (Figure 5) and subarray 8-11 (Figure 8) suggests that, despite the lack of redundancy in the seismogeodetic inversion for three-station arrays, strains and rotations inferred from arrays 1-3 and 8-11 are comparable in magnitude to those from array 5-12. Although the time series in Figures 4, 5, and 8 differ in detail, they show comparable amplitudes (as summarized in Table 3), and they show some of the same pulses (e.g. at 36 s). Given that site effects might be contributing misfits equal to the amplitude of the uniform strain "signal" (i.e. misfit ratio is 0.4 - 0.5), this degree of variation between the results of different arrays is not surprising and is consistent with the results of Suryanto et al. (2006). A comparison of peak torsions inferred in various bands from various subarrays is shown in Figure 9. From the agreement of the peak motions of the different subarrays in the 0.1 - 1.4 Hz band, we infer that strains and rotations inferred from the small arrays 1-3 and 8-11 in the wider 0.1 - 3.6 Hz band will be accurate to a factor of about two or better

In Figure 7 we show the time series for the smallest aftershock, the M4.7 2721724 event. As this event has the smallest motions it represents our least well-determined result. We infer little from it, although we assume, based on the previous discussion, that its peak values are in error by a factor of two or less. Time series plots for other events and arrays are not shown.

Fourier spectra of torsions, and comparison with velocity

It has long been known that spatial and temporal derivatives of the seismic wave field on the Earth's surface are related through the horizontal phase velocity *c* (e.g. Benioff and Gutenberg, 1952), and Igel et al. (2005) has shown specifically that

$$\omega_3 = -\dot{u}/(2c), \qquad (1)$$

where $\dot{u}$ is the transverse horizontal component of velocity. Our data agree with Igel's relationship, as shown by the comparison of torsion and velocity spectra shown in Figure 10 for the mainshock and 2731710 aftershock recorded on the 5-12 array. To produce the plotted velocity spectrum, for each station the vector sum of the amplitude spectra of the two components for each entire record was taken. The plotted spectrum is the average over all stations of these vector sums. In Figure 10 the torsion spectra have been multiplied by 2.9 km/s, which implies an average phase velocity of 1.45 km/s during the entire record, including S wave and coda. This number is comparable to but slightly lower than the 2.0 - 2.75 km/s phase velocities inferred by Fletcher et al. (2006) during the mainshock S waves

Estimation of broadband strains and rotations

Recall that to satisfy the uniform strain assumption we have low-pass filtered the ground motion data to remove signals with seismic wavelength λ, measured along the Earth's surface, shorter than $4h$, where h is the horizontal extent of the array. We would like to correct our band-limited rotations in order to estimate broadband peak rotations. We have developed some simple correction factors to accomplish this. Figure 11 compares velocity and scaled torsion amplitude spectra from array 1-3 filtered in the 0.1 - 3.6 Hz band. It suggests that the 0.1 - 3.6 Hz band captures most of the energy in the torsion spectrum, because the spectra of both events are decaying above 2 Hz, which is below the 3.6 Hz corner frequency where the filter is down by a factor of two. This implies that small corrections to the peak rotations inferred from the 0.1 - 3.6 Hz band might be good estimates of the broadband peak rotations. Figures 10 and 11 both show that the torsion spectra are very similar to the ground velocity spectra, and presumably the torsion rate spectra are very similar to the ground acceleration spectra. Consequently, as a multiplicative factor to correct our band passed peak rotation data, we have calculated the ratio of peak ground velocity (PGV) inferred from unfiltered ground velocity to PGV from band passed ground velocity. We use a similar ratio of unfiltered to band passed PGA as a correction factor for peak rotation rates. The specific calculation procedure is given in Appendix B. The correction factors used for various combinations of subarray, pass band, and event are shown in Table 4. Broadband peak rotations, rotation rates, strains, and dilatations are given in Table 5,

which is obtained by multiplying values from the 1-3 (3.6 Hz), 8-11 (3.6 Hz), and 5-12 (1.4 Hz) arrays in Table 3 by the appropriate correction factor in Table 4 and averaging the results. Table 5 contains our best estimates of the strains and rotations observed by UPSAR.

Our main shock peak dilatation, about 5.6 microstrain (Table 5), agrees with peak main shock dilatation measured by Johnston et al. (2006) to about a factor of slightly more than two. They obtained peak dilatations of about 15, 10, 13, and 40 microstrain (their Figure 4) on downhole dilatometers at stations Donna Lee, Froelich, Red Hills, and Vineyard Canyon, at distances of about 5, 3, 15, and 20 km, respectively, from the rupture. With the exception of the Vineyard Canyon measurement, our dilatation is a factor of 2.3 lower than theirs, surprisingly good agreement given the completely different measurement methods.

Our main shock horizontal shear strain, 88 microstrain, is about a factor of two lower than the horizontal principle strains derived from UPSAR main shock data by Paolucci and Smerzini (2008), primarily because their strains include horizontal dilatation, which can be seen from Table 5 to be comparable in amplitude to the horizontal shear strains. Secondarily, their strains include the effects of site amplification, which is also included in our 3-station subarray strains but it not included in our subarray 5-12 strains. The horizontal shear strains for all our events in Table 5 fall between the scaling lines in Paolucci and Smerzini's Figure 7.

Scaling of rotations with seismic moment and distance

Our observation that Igel's relationship (1) works pretty well (e.g. Figure 10) leads us to speculate that peak rotation and rotation rates might scale with magnitude, distance, site geology, and fault type like the scaling of peak velocity and peak acceleration in empirical ground motion prediction relationships like Boore and Atkinson (2007). A similar comparison for teleseismic distances has been done by Igel et al. (2007). In Figure 12 we show our broad-band corrected measurements (Table 5) as a function of moment, along with the near-source measurements of Huang (2003) on the 1999 M_w7.6 Chi-Chi earthquake, the near-source measurements of Takeo (1998) on M_w 5.4 and 4.9 events off Ito, Japan, and theoretical torsions and torsion rates from Bouchon and Aki (1982). Huang measured rotation and rotation rate around the three axes. Takeo measured only rotation rate around all three axes. To calculate their tilts for Figure 12, we took the Pythagorean sum of their rotations around horizontal axes. Plotted values from

Bouchon and Aki were from their calculations at station 3, 10 km from the center of their 30-km-long vertical strike-slip fault. This station's location relative to the fault is almost identical to UPSAR's location relative to the Parkfield mainshock.

Shown by crosses in Figure 12 are the rotations we have obtained from the Boore-Atkinson (BA) relations by dividing predicted horizontal PGA and PGV by c = 1000 m/s to get peak torsion and torsion rate, respectively. Specifically, the crosses are

(peak rotation) = (PGV, m/s, from BA) / (2c), c = 1000 m/s (2a)

(peak rotation rate) = (PGA, m/s^2, from BA) / (2c), c = 1000 m/s (2b)

The value of phase velocity c was chosen by eye rather than a least-squares procedure. When evaluating the BA peak motions, we used the seismic moments, mechanisms, Joyner-Boore distances, and surficial shear velocities reported in the Huang, Takeo and Bouchon papers, in Fletcher et al. (2006) and in Table 1, except that we guessed a surficial shear velocity of 600 m/s for Huang's array (a reasonable guess, B.S. Huang, personal communication, 2007), which partially straddled an earth- and rock-fill dam. The BA relations are for only horizontal motions, so they are most appropriately compared with torsions and torsion rates. The prediction error of the BA relations is about a factor of 1.75.

Several observations can be made regarding Figure 12. First, the torsion/tilt ratio seems to be correlated with event mechanism. Considering the UPSAR Parkfield measurements, torsions and torsion rates are always greater than tilts and tilt rates. The observed torsion/tilt ratio is very similar to the theoretical ratio shown in Figure 12 obtained by Bouchon and Aki for their vertical strike-slip fault. As the UPSAR vertical peak motions are on the average half the horizontal peaks, we might expect torsions to be about twice the tilt, but the observed ratio is less than two. For Chi-Chi peak torsion approximately equals peak tilt, and peak torsion rate approximately equals peak tilt rate, possibly related to the reverse mechanism of that event. However, tilt rates are much greater than torsion rates for Takeo's Ito, Japan, events, which are dike-injection events (M. Takeo, personal communication, 2007) having significant non-double-couple components, recorded on a Systron-Donner Motion-Pak triaxial gyro rotation-rate sensor.

Second, Figure 12a shows that near-source peak torsions and tilts for Parkfield and Chi-Chi are well predicted using relationship (2) over the M_w range 4.7 - 7.6. Figure 12b shows that use of (2) predicts the Parkfield torsion rates and tilt rates reasonably well except for the smallest event (factor of 3 overprediction) and for Chi-Chi, which is overpredicted by a factor of 5. However, equation (2) underpredicts Takeo's measurements from Ito, Japan, by factors ranging from 5 to 60. The relation overpredicts Bouchon and Aki's torsion rate, but poor agreement is expected because their calculation was band-limited to the 0 - 2.5 Hz band and their source had uniform slip, so it could not possibly yield a realistic estimate of peak ground acceleration and hence peak torsion rate.

Discussion

The main contributions of this paper are our near-source observations of strains, rotations, and rotations rates (Table 5) from a moderate magnitude earthquake and its larger aftershocks. We have also shown (Figure 12) that equation (2) can be a useful predictor of peak rotations and rotation rates, at least for events having small non-double-couple components.

The biggest surprise in Figure 12 is the complete disagreement between Takeo's point measurements of rotation rates from the Ito, Japan, events, and our array-derived observations and predictions from (2) (Figure 12b). This discrepancy is unlikely to be caused by inaccuracies in Takeo's observations because subsequent comparisons of MotionPak data with that from a higher sensitivity sensor show good agreement (Takeo, 2007). Takeo (1998) attributed the large discrepancy between his and Bouchon and Aki's rotation rates to the rotational motions contributed from spatial variation of slip at the source, a factor lacking in the Bouchon and Aki calculation. However, presumably the Parkfield aftershocks have spatially variable slip, so the rotation rates of these events should agree with the Ito, Japan, events.

Three possible explanations of the discrepancy are that 1) the rotations predicted by equation (2) are biased low for the Ito events, or 2) point measurements are affected by heterogeneities in the soil structure with wavelengths of a few meters, so that local meter-scale rotations are much greater than rotations averaged over tens or hundreds of meters, and/or 3) that

events with significant non-double-couple mechanisms, like the Ito events, radiate much greater rotations than the double-couple Parkfield events (M. Takeo, personal communication, 2007).

Explanation 1, that the predictions are biased low, could occur if we used the wrong epicentral distance or surface shear wave velocity (or some other input factor) in the Boore-Atkinson (BA) relation. (Because the Ito events occur in an extensional region, we used the BA predictions for normal-faulting events.) To answer this question, we have also performed a preliminary analysis of two additional 1998 Ito events presented by Takeo (2007), April 25, 2237 UTC (M_w 5.0, FNET), and April 26, 0603 UTC (M_w 4.6), assumed to be at an epicentral distance of 3.3 km from station KAW. The BA relation predicts observed peak acceleration for three of the four Ito events with an error of less than one standard deviation. The BA prediction for the fourth event (19970621409) is a factor of 3 low. Consequently, the discrepancy between equation (2) and the observed 1997 Ito rotation rates is not explained by a biased BA prediction of PGA.

There is some evidence supporting explanation 2, that the rotation is scale-dependent, but it is not compelling. We have previously noted that our array-determined dilatations agree with the dilatometer observations of Johnston et al. (2006) to about a factor of 2.3. Suryanto et al. (2006) have shown excellent agreement of point- and array-measurements of rotational motions, but these were long-wavelength teleseismic observations. It is possible that lateral variations in geology and site effects are a significant contributor to local rotations. The misfit ratio during the Parkfield mainshock S wave (Figure 4, 24-30 s) is about 0.5, meaning that half of the observed interstation displacements are not explained by a rigid rotation and uniform strain. We speculate that lateral variations in site effects contribute the unmodeled displacements. There is probably some correlation length associated with site effects, with this length being controlled both by the seismic wavelength and by the correlation length of the local geology. At the UPSAR site, that correlation length might be rather short, as illustrated by the surprising amount of variation between the ground motions recorded at sites 5, 6, and 7, 25 - 40 m apart from each other (Fletcher et al., 2006, Figure 2). If site effects were truly uncorrelated from station to station, ground rotations and strains would be proportional to 1/(array dimension). Of course, at some small station separation the site effects are correlated, becoming identical at zero separation. We speculate that rotations inferred from arrays will grow as array dimension decreases, and then will converge to the point rotation measurement as the dimension descends

from the correlation length to zero. Some weak evidence of larger rotations over shorter array dimensions is given in Table 6. Each cell of this table shows the ratio of the average of the 1-3 array and the 8-11 array values of a quantity (peak torsion, for example) to the 5-12 array value of that quantity. Thus, the average peak torsion measured over all events on the 1-3 and 8-12 arrays is 1.18 times the average peak torsion of all events measured on the 5-12 array. Tilt in the small arrays is 19% larger than in the 5-12 array. Unfortunately we could not calculate a stable rotation from the 5, 6, 7 subarray to check our speculation. In summary, the significant variations in ground motions among stations 5, 6, and 7 support the hypothesis of a scale-dependent rotation, but the good agreement of our array-derived dilatations with the point dilatometer observations does not support the hypothesis.

The more interesting possibility is that non-double-couple sources produce greater rotations than do double-couple sources, as suggested by the large exceedence of the observed Ito rotation rates compared to the predictions of equation (2). These are dike injection events (M.Takeo, personal communication, 2007), with the larger 0351 event having a 29% or 74% double-couple component (CMT catalog and FNET catalog, respectively), and with the smaller 1409 event having a 58% double-couple mechanism (FNET). In general all four Ito events that we have studied appear to have a higher ratio of peak rotation / PGV or peak rotation rate / PGA than do the Parkfield and Chi-Chi events. Equation (2) can be rearranged to produce estimates of apparent velocity c from ratios of observed PGA or PGV to observed peak rotation rate or peak rotation, respectively. This c is not necessarily a true phase velocity, but is rather a scaling factor relating rotation to translation. For the four Ito events it ranges from about 50 to 375 m/s, whereas for the Parkfield events it ranges from about 700 to 1700 m/s. Consequently, it appears that the Ito events have a larger ratio of rotation to translation than do the Parkfield events.

If it is true that non-double-couple events radiate much greater rotational motions than double couple events for comparable levels of translation, then rotational observations might provide an important source of new information for monitoring seismicity in volcanic areas.

Finally, estimates of apparent velocity c formed from ratios of observed PGA or PGV to observed peak rotation rate or peak rotation might be useful indicators of permanent tilts in seismic records. Graizer (2006) inferred a permanent ground tilt from the Pacoima Upper Left Abutment accelerogram of the 1971 San Fernando earthquake. This tilt was confirmed by direct observation of the site. Estimates of c that we formed from translation/rotation ratios for this

record are in the 50 - 150 m/s range, much less than the 700 - 1700 m/s range of Parkfield events. Such low apparent velocities for a tectonic earthquake may be an indicator of permanent tilt caused by soil failure.

Appendix A. Derivation of rotations and strains

The basic derivation of the "seismogeodetic" method is given in Appendix A of Spudich et al. (1995). In this appendix we summarize the equations that define the rotational quantities plotted in the figures. Definitions not explicitly given here can be found in S95.

The solution $\tilde{\mathbf{p}}$ for the unknown displacement gradient vector $\mathbf{p} = \left(u_{1,1}\ u_{1,2}\ u_{1,3}\ u_{2,1}\ u_{2,2}\ u_{2,3}\right)^T$ is $\tilde{\mathbf{p}}(t) = g\mathbf{d}(t)$ from S95(A5). $\mathbf{d}(t)$ is the data vector, i.e. the vector of relative station offsets at time t, g is the generalized inverse matrix given by $g = \left(A^T C_d^{-1} A\right)^{-1} A^T C_d^{-1}$, where C_d, the data covariance matrix, and A are defined in S95. Because of the free surface boundary conditions, which determine $u_{3,i}$ from the other displacement gradients, the displacement gradient matrix $U(t)$ is determined from solution $\tilde{\mathbf{p}}(t)$ by

$$U = \begin{pmatrix} \tilde{p}_1 & \tilde{p}_2 & \tilde{p}_3 \\ \tilde{p}_4 & \tilde{p}_5 & \tilde{p}_6 \\ -\tilde{p}_3 & -\tilde{p}_6 & -\eta\left(\tilde{p}_1 + \tilde{p}_5\right) \end{pmatrix} \qquad \text{(A1)}$$

where $\tilde{p}_i$ is the i-th element of $\tilde{\mathbf{p}}$, and where the time dependence is understood. Elements of the rotation tensor are $\omega_{ij} = \left(U_{ji} - U_{ij}\right)/2$. The k-th element of the rotation vector $\boldsymbol{\omega}$ is $\omega_k = e_{kij}\omega_{ij}$, where e_{kij} is the alternating tensor. Combination of these relations yields rotation vector elements $\omega_1 = -\tilde{p}_6$, $\omega_2 = \tilde{p}_3$, and $\omega_3 = \left(\tilde{p}_4 - \tilde{p}_2\right)/2$. Torsion is ω_3, rotation about the vertical axis. Tilt, defined here as $\sqrt{\omega_1^2 + \omega_2^2}$, is rotation about a horizontal axis. Note that with this

definition, the axis about which tilt occurs changes with time during the motion (i.e. the local uphill direction rotates randomly during the shaking), and tilt is non-negative. Elements of the strain tensor are $e_{ij} = \left(U_{ji} + U_{ij}\right)/2$. The strain tensor has eigenvalues $\lambda_1 \geq \lambda_2 \geq \lambda_3$. Dilatation $d = e_{11} + e_{22} + e_{33}$, and the maximum shear strain across any plane is $s = \left(\lambda_1 - \lambda_3\right)/2$. Because building foundations are typically wider than their depth of embedment, we consider also strain in the horizontal plane,

$$e^h = \begin{pmatrix} e_{11} & e_{12} \\ e_{21} & e_{22} \end{pmatrix}.$$

Horizontal dilatation $d^h = e_{11} + e_{22}$, and eigenvalues of the horizontal strain tensor are $\lambda_1^h \geq \lambda_2^h$. Maximum shear strain across any vertically oriented plane is $s^h = \left(\lambda_1^h - \lambda_2^h\right)/2$. Formal error estimates may be derived as follows. The solution covariance matrix is $C_p = g C_d g^T$, and the variance of $\tilde{p}_i$ is $\left(C_p\right)_{ii}$. Consequently, the standard deviations of ω_1, ω_2, and ω_3 are, respectively, $\sigma_{\omega_1} = \sqrt{\left(C_p\right)_{66}}$, $\sigma_{\omega_2} = \sqrt{\left(C_p\right)_{33}}$, and $\sigma_{\omega_3} = \frac{1}{2}\sqrt{\left(C_p\right)_{22} - 2\left(C_p\right)_{24} + \left(C_p\right)_{44}}$. Finally, from S95 the data covariance matrix $C_d = DC_uD^T$, where D is defined in S95 and where C_u is the diagonal displacement covariance matrix. Stations 11, 12, and 13 of the UPSAR array had noisier digitizers than the other stations. We measured the variance of displacement ground noise at the quieter and noisier stations to be 4.05e-6 cm and 2.47 e-5 cm, respectively. We inserted these values into the appropriate diagonal element of C_u for each station.

A final subtlety warrants discussion. We follow S95 in making two slightly inconsistent assumptions. We assume that all stations are on the free surface, which they are. The free-surface boundary condition assumes that the surface is flat. However, UPSAR is in a hilly area, and the stations are at different elevations, so that we use the actual elevation difference Δz between two stations when terms such as du/dz are calculated. Because the elevation differences between the stations are much less than the seismic wavelengths, we believe that the assumption of flatness of the free surface is essentially correct.

Appendix B. Broadband Correction Factors

For each component of motion at each UPSAR station, we calculated the ratio of filtered to unfiltered peak motion (PGV and PGA) for both pass bands used (1.4 and 3.6 Hz) for the mainshock and for the 2731710 aftershock. We averaged the peak motion ratios over all stations. The torsion (torsion rate) correction was taken to be the inverse of the average of the two horizontal PGV (PGA) average ratios. Since tilt is caused by vertical motions, the tilt (tilt rate) correction was simply taken to be the average ratio of the filtered to unfiltered vertical component PGV (PGA). Because the maximum shear strain and the maximum dilatation occur during the S and coda waves, not during the P waves, we corrected shear strain and dilatation using the torsion correction factor. Our correction factor for the 0.1 - 3.6 Hz band for main shock torsion, shear strain, and dilatation, 1.18, agrees well with with the 1.09 and 1.16 ratios of unfiltered to filtered main shock dilatations presented by Borcherdt et al. (2006; his Figures 8 and 9) for stations Froelich and Donna Lee, respectively.

Acknowledgements.

We thank Lawrence M. Baker and Russell W. Sell for their help in data collection and management. W.H.K. Lee stimulated our renewed interest in rotation measurements. We thank W.H.K. Lee, J.R. Evans, H. Igel, and P. Bodin for helpful reviews, and we thank M. Takeo for important suggestions.

Table 1. Parkfield area earthquake parameters

Event name	Time	Lat	Lon	depth (km)	M_w	Rjb(km)
2721715	2004 272 1715:24	35.815	-120.374	7.9	6.0	8.8
2721724	2004 272 1724:15	35.806	-120.349	6.7	4.7	14.0
2731710	2004 273 1710:04	35.953	-120.502	11.5	5.1	14.4
2741854	2004 274 1854:28	35.984	-120.550	10.1	4.9	18.3

Table 2. Low-pass corner frequency appropriate for each subarray

Subarray	h (m)	f_{max} (Hz)
5, 6, 7	30	16.7
1,2,3 or 8,9,11	140	3.6
5,6,7,8,9,11,12	350	1.4
whole array	900	0.55

Table 3. Observed band-limited peak values for rotations and strains, all events

	Array	f_{max} (Hz)	**main**	**2721724**	**2731710**	**2741854**
total dilatation	1-3	1.4	2.28E-06	1.20E-07	2.40E-07	1.77E-07
total shear strain	1-3	1.4	4.47E-05	2.05E-06	4.84E-06	2.94E-06
horiz. dilatation	1-3	1.4	4.00E-05	2.10E-06	4.21E-06	3.10E-06
horiz. shear strain	1-3	1.4	3.61E-05	1.76E-06	4.02E-06	2.62E-06
torsion (rad)	1-3	1.4	2.25E-05	1.64E-06	3.48E-06	2.73E-06
torsion rate (rad/s)	1-3	1.4	1.39E-04	9.12E-06	2.10E-05	1.23E-05
tilt (rad)	1-3	1.4	2.18E-05	1.51E-06	3.51E-06	1.83E-06
tilt rate (rad/s)	1-3	1.4	1.45E-04	8.82E-06	1.64E-05	9.46E-06
total dilatation	1-3	3.6	4.34E-06	1.70E-07	6.42E-07	4.17E-07
total shear strain	1-3	3.6	9.13E-05	2.77E-06	1.12E-05	6.83E-06
horiz. dilatation	1-3	3.6	7.61E-05	2.98E-06	1.13E-05	7.31E-06
horiz. shear strain	1-3	3.6	7.10E-05	2.77E-06	8.66E-06	6.83E-06
torsion (rad)	1-3	3.6	5.11E-05	1.94E-06	7.81E-06	5.99E-06
torsion rate (rad/s)	1-3	3.6	5.23E-04	2.20E-05	1.09E-04	7.50E-05
tilt (rad)	1-3	3.6	4.09E-05	2.36E-06	7.62E-06	4.79E-06
tilt rate (rad/s)	1-3	3.6	3.81E-04	1.93E-05	8.52E-05	5.52E-05
total dilatation	8-11	1.4	2.15E-06	9.64E-08	3.82E-07	2.97E-07
total shear strain	8-11	1.4	5.84E-05	1.97E-06	5.70E-06	4.89E-06
horiz. dilatation	8-11	1.4	3.77E-05	1.69E-06	6.69E-06	5.20E-06
horiz. shear strain	8-11	1.4	3.92E-05	1.97E-06	4.34E-06	2.61E-06
torsion (rad)	8-11	1.4	6.17E-05	1.88E-06	5.14E-06	5.67E-06
torsion rate (rad/s)	8-11	1.4	4.48E-04	1.08E-05	3.22E-05	2.69E-05
tilt (rad)	8-11	1.4	3.54E-05	1.89E-06	4.24E-06	3.00E-06
tilt rate (rad/s)	8-11	1.4	2.20E-04	8.17E-06	2.18E-05	1.95E-05
total dilatation	8-11	3.6	6.48E-06	1.79E-07	8.82E-07	1.06E-06
total shear strain	8-11	3.6	1.31E-04	3.18E-06	1.57E-05	1.61E-05
horiz. dilatation	8-11	3.6	1.14E-04	3.14E-06	1.55E-05	1.86E-05
horiz. shear strain	8-11	3.6	9.31E-05	2.90E-06	1.35E-05	1.16E-05
torsion (rad)	8-11	3.6	1.11E-04	2.42E-06	1.68E-05	1.01E-05
torsion rate (rad/s)	8-11	3.6	1.24E-03	3.01E-05	2.27E-04	8.79E-05
tilt (rad)	8-11	3.6	7.93E-05	2.32E-06	1.59E-05	7.88E-06
tilt rate (rad/s)	8-11	3.6	6.41E-04	2.27E-05	1.68E-04	8.66E-05
total dilatation	5-12	1.4	1.89E-06	1.10E-07	2.35E-07	1.45E-07
total shear strain	5-12	1.4	3.43E-05	1.99E-06	4.14E-06	4.40E-06
horiz. dilatation	5-12	1.4	3.31E-05	1.92E-06	4.12E-06	2.55E-06
horiz. shear strain	5-12	1.4	3.43E-05	1.49E-06	3.10E-06	2.74E-06
torsion (rad)	5-12	1.4	3.56E-05	1.43E-06	4.42E-06	3.16E-06
torsion rate (rad/s)	5-12	1.4	2.23E-04	7.47E-06	2.49E-05	1.64E-05
tilt (rad)	5-12	1.4	2.54E-05	1.50E-06	3.23E-06	1.88E-06
tilt rate (rad/s)	5-12	1.4	9.50E-05	6.55E-06	1.48E-05	9.18E-06

Table 4. Peak rotation and rotation rate correction factors for event/array combinations

	mainshock		aftershocks
band (Hz)	0.1-1.4	0.1-3.6	0.1-3.6
subarray	5-12	1-3 & 8-11*	1-3 & 8-11*
torsion	2.06	1.18	1.49
tilt	2.25	1.24	1.67
torsion rate	4.33	1.30	2.43
tilt rate	7.54	2.01	3.09

* Results from subarrays 1-3 and 8-11 are averaged

Table 5. Broadband estimates of Parkfield peak rotations and strains

	main	2721724	2731710	2741854
total dilatation	5.55E-06	3.67E-07	1.17E-06	9.90E-07
total shear strain	1.11E-04	6.47E-06	2.07E-05	1.92E-05
horiz. dilatation	9.72E-05	6.44E-06	2.05E-05	1.73E-05
horiz. shear strain	8.80E-05	5.45E-06	1.65E-05	1.40E-05
torsion (rad)	8.81E-05	4.69E-06	2.00E-05	1.36E-05
torsion rate (rad/s)	1.09E-03	9.44E-05	4.46E-04	2.47E-04
tilt (rad)	6.89E-05	4.74E-06	1.77E-05	9.73E-06
tilt rate (rad/s)	9.25E-04	9.26E-05	3.72E-04	2.15E-04

Table 6. Ratios of (average * for three-station arrays)/(measured * for 5-12) in 0.1-1.4 Hz band

*	mainshock	2741854	2731710	2721724	row average
torsion	1.18	1.33	0.97	1.23	1.18
torsion rate	1.32	1.19	1.07	1.33	1.23
tilt	1.13	1.29	1.20	1.14	1.19
tilt rate	1.92	1.58	1.29	1.30	1.52
column average	1.39	1.35	1.13	1.25	

References

Benioff, H., and B. Gutenberg (1952). The response of strain and pendulum seismographs to surface waves, *Bull. Seism. Soc. Am.*, **43**, 229 - 237.

Bodin, P., J. Gomberg, S. K. Singh, and M. Santoyo (1997). Dynamic deformations of shallow sediments in the Valley of Mexico, Part I: Three-dimensional strains and rotations recorded on a seismic array, *Bull. Seism. Soc. Am.*, **87**, 528 - 539.

Borcherdt, R., M. Johnston, G. Glassmoyer, and C. Dietel (2006). Recordings of the 2004 Parkfield earthquake on the General Earthquake Observation System Array: Implications for earthquake precursors, fault rupture, and cosesmic strain changes, *Bull. Seism. Soc. Am.,* **96**, S73-S89, doi: 10.1785/0120050827.

Boore, D.M, and G.M. Atkinson (2007). Ground motion prediction equations for the average horizontal component of PGA, PGV, and 5% damped SA at spectral periods between 0.01 s and 10.0 s, available from http://quake.wr.usgs.gov/~boore/pubs_online/ba_nga_gmpes_main_v3.04.pdf.

Bouchon, M., and K. Aki (1982). Strain, tilt, and rotation associated with strong ground motion in the vicinity of earthquake faults, *Bull. Seism. Soc. Am.*, **72**, 1717-1738.

Fletcher, J., L.M. Baker, P. Spudich, P. Goldstein, J.D. Sims, and M.Hellweg (1992). The USGS Parkfield, California, dense seismograph array-UPSAR*, Bull. Seism. Soc. Am.,* **82**, 1041-1070.

Fletcher, J., P. Spudich, and L.M. Baker (2006). Rupture propagation of the 2004 Parkfield, California, earthquake from observations at the UPSAR, *Bull. Seism. Soc. Am.,* **96**, S129-S142, doi: 10.1785/0120050812.

Graizer, V. (2006). Tilt in strong ground motion, *Bull. Seism. Soc. Am.,* **96**, 2090-2102, doi: 10.1785/0120060065.

Huang, B.-S. (2003). Ground rotational motions of the 1999 Chi-Chi, Taiwan, earthquake as inferred from dense array observations, *Geophys. Res. Let*., **30**, 40-1 - 40-4, doi: 10.1029/2002GL015157.

Igel, H., U. Schreiber, A. Flaws, B. Schuberth, A. Velikoseltsev, and A. Cochard (2005). Rotational motions induced by the M8.1 Tokachi-oki earthquake, September 25, 2003, *Geophys. Res. Let*., **32,** L08309, doi:10.1029/2004GL022336.

Igel, H., A. Cochard, J. Wassermann, A. Flaws, U. Schreiber, A. Velikoseltsev, and N. Dinh (2007). Broad-band observations of earthquake-induced rotational ground motions, *Geophys. J. Int*., **168**, 182-196, doi: 10.1111/j.1365-246X.2006.03146.x.

Johnston, M.J.S., R.D. Borcherdt, A.T. Linde, and M.T. Gladwin (2006). Continuous borehole strain and pore pressure in the near field of the 28 September 2004 M 6.0 Parkfield, California, earthquake: Implications for nucleation, fault response, earthquake prediction, and tremor, *Bull. Seism. Soc. Am.,* **96**, S56-S72, doi: 10.1785/0120050822.

Liu, P., S. Custodio, and R. Archuleta (2006). Kinematic inversion of the 2004 M 6.0 Parkfield earthquake including an approximation of site effects, *Bull. Seism. Soc. Am.,* **96**, S143-S158, doi: 10.1785/0120050826.

Mikumo, T., and K. Aki (1964). Determination of local phase velocity by intercomparison of seismograms from strain and pendulum instruments, *J. Geophys. Res*., **69**, 721-731.

Oliveira, C.S., and B.A. Bolt (1989). Rotational components of surface strong ground motion, *Earthq. Eng. Struct. Dyn*., **18**, 517-526.

Paolucci, R., and C. Smerzini (2008). Earthquake-induced transient ground strans from dense seismic networks, *Earthq. Spectra*, in press.

Spudich, P., L.K Steck, M. Hellweg, J. Fletcher, and L.M. Baker (1995). Transient stresses at Parkfield, California, produced by the M7.4 Landers earthquake of June 28, 1992: observations from the UPSAR dense seismograph array, *J. Geophys. Res*. **100**, 675-690.

Suryanto, W., H. Igel, J. Wassermann, A. Cochard, B. Schuberth, D. Vollmer, F. Scherbaum, U. Schreiber, and A. Velikoseltsev (2006). First comparison of array-derived rotational ground motions with direct ring laser measurements, *Bull. Seism. Soc. Am.,* **96**, 2059-2071, doi: 10.1785/0120060004.

Takeo, M. and H.M. Ito (1997). What can be learned from rotational motions excited by earthquakes, *Geophys. J. Int*., **129**, 319-329.

Takeo, M. (1998). Ground rotational motions recorded in the near-source region of earthquakes, *Geophys. Res. Let*., **25**, 789-792.

Takeo, M. (2007). Rotational motions observed during an earthquake swarm in April, 1998, at Offshore Ito, Japan, Abstracts with Program, First Internat. Workshop on Rotational Seismology and Engineering Applications, Menlo Park, CA, Sept. 18-19, 2007.

Trifunac, M.D. (1982). A note on rotational components of earthquake motions for incident body waves, *Int. J. Soil Dynamics and Earthquake Engineering*, **1**, 11-19.

Wang, G-Q., G-Q. Tang, C.R. Jackson, X-Y. Zhou, and Q-L. Lin (2006). Strong ground motions observed at the UPSAR during the 2003 San Simeon (M 6.5) and 2004 Parkfield (M 6.0), California, earthquakes, *Bull. Seism. Soc. Am.,* **96**, S159-S182, doi: 10.1785/0120050802.

Figure Captions

Figure 1. Map of the array stations. Gray lines indicate subarrays 1-3 and 8-11. Gray loop surrounds subarray 5-12 stations.

Figure 2. Map showing location of UPSAR (square) relative to the San Andreas and the mainshock (heavy cross) and aftershock (light crosses) epicenters.

Figure 3. Error of approximating true tangent angle ϕ_t by the slope angle ϕ_c of the chord. x axis is horizontal position, y axis is ground displacement. Stations 1 and 2 are separated by horizontal distance h. Solid line is the ground displacement at a particular instant of time.

Figure 4. Calculated strains and rotations for the mainshock using stations 5-12 in the band 0.1 - 1.4 Hz. Row 1 is maximum shear strain across a vertical plane (solid) and total dilatation (dashed). Row 2 is torsion, row 3 is torsion rate, row 4 is tilt, row 5 is tilt rate, row 6 is the misfit ratio, and row 7 is the station P05 north component of velocity.

Figure 5. Calculated strains and rotations for the mainshock using stations 1 - 3 in the band 0.1 - 1.4 Hz. Row 1 is maximum shear strain across a vertical plane (solid) and total dilatation (dashed). Row 2 is torsion, row 3 is torsion rate, row 4 is tilt, row 5 is tilt rate, row 6 is the misfit ratio (which is essentially zero because the inversion is even-determined), and row 7 is the station P01 north component of velocity.

Figure 6. Calculated strains and rotations for the mainshock using stations 1 - 3 in the band 0.1 - 3.6 Hz. Row 1 is maximum shear strain across a vertical plane (solid) and total dilatation (dashed). Row 2 is torsion, row 3 is torsion rate, row 4 is tilt, row 5 is tilt rate, row 6 is the station P01 north component of velocity.

Figure 7. Calculated strains and rotations for the M4.7 2721724 event using stations 8 - 11 in the band 0.1 - 3.6 Hz. Row 1 is maximum shear strain across a vertical plane (solid) and total dilatation (dashed). Row 2 is torsion, row 3 is torsion rate, row 4 is tilt, row 5 is tilt rate, row 6 is the station P08 north component of velocity.

Figure 8. Calculated strains and rotations for the mainshock using stations 8 - 11 in the band 0.1 - 1.4 Hz. Row 1 is maximum shear strain across a vertical plane (solid) and total dilatation (dashed). Row 2 is torsion, row 3 is torsion rate, row 4 is tilt, row 5 is tilt rate, and row 6 is the station P08 north component of velocity.

Figure 9. Peak torsions of the four Parkfield events and their dependence on bandwidth. Measurements are from arrays 1-3 (gray), 8-11 (black), and 5-12 (asterisk). Squares are results for the 0.1 - 3.6 Hz band, crosses and asterisks are for the 0.1 -1.4 Hz band.

Figure 10. Fourier amplitude spectra of velocity (solid) and scaled torsion (dashed) for the mainshock and the 2731710 aftershock as inferred on array 5-12 filtered with corners at 0.1 and 1.4 Hz. Velocity spectra are averages over all stations of the vector sum of the amplitude spectra of both horizontal components. Scaled torsions are torsions multiplied by 2.9 km/s, implying a phase velocity of 1.45 km/s.

Figure 11. Fourier amplitude spectra of velocity (solid) and scaled torsion (dashed) for the mainshock (solid lines) and the 2731710 aftershock (dashed lines), as inferred on array 1-3 filtered with corners at 0.1 and 3.6 Hz. Velocity spectra are averages over all stations of the vector sum of the amplitude spectra of both horizontal components. Scaled torsions are torsions multiplied by 2 × 1.45 km/s. Amplitude spectra decay rapidly above 2 Hz, suggesting that most torsion power is found below 3.6 Hz.

Figure 12. Comparisons of a) torsions (black) and tilts (gray), and b) torsion rates (black) and tilt rates (gray) as functions of source moment for Parkfield, Taiwan, and Japan events. Circles are averages of Parkfield subarray 1-3, 8-11, and 5-12 measurements corrected to broadband (Table 5). Crosses are predictions based on equation (2). Observations (triangles) from Chi-Chi, Taiwan, Ito, Japan, and simulations (diamonds) from Bouchon and Aki (1982) are shown.

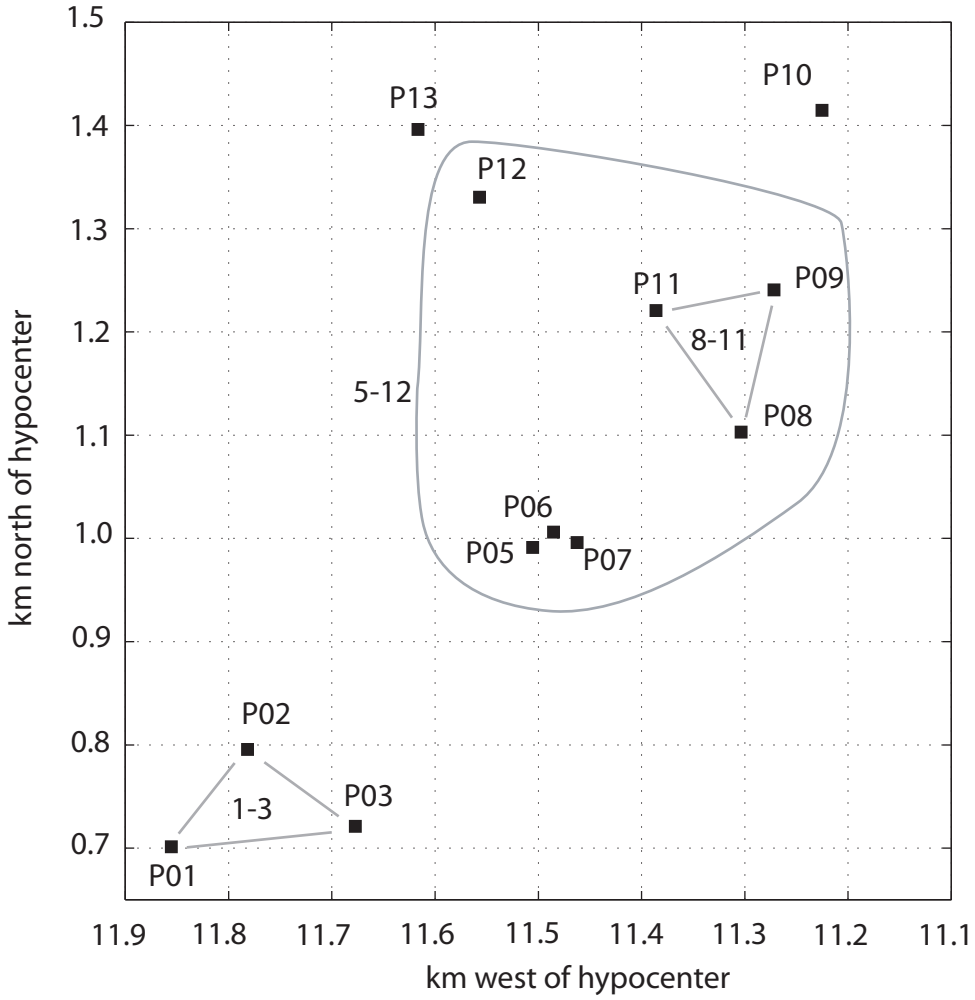
1.5
1.4
1.3
1.2
1.1
1.0
0.9
0.8
0.7
km north of hypocenter
11.9
11.8
11.7
11.6
11.5
11.4
11.3
11.2
11.1
km west of hypocenter
P13
P10
P12
P11
P09
8-11
5-12
P08
P06
P05
P07
P02
P03
1-3
P01

Figure 1

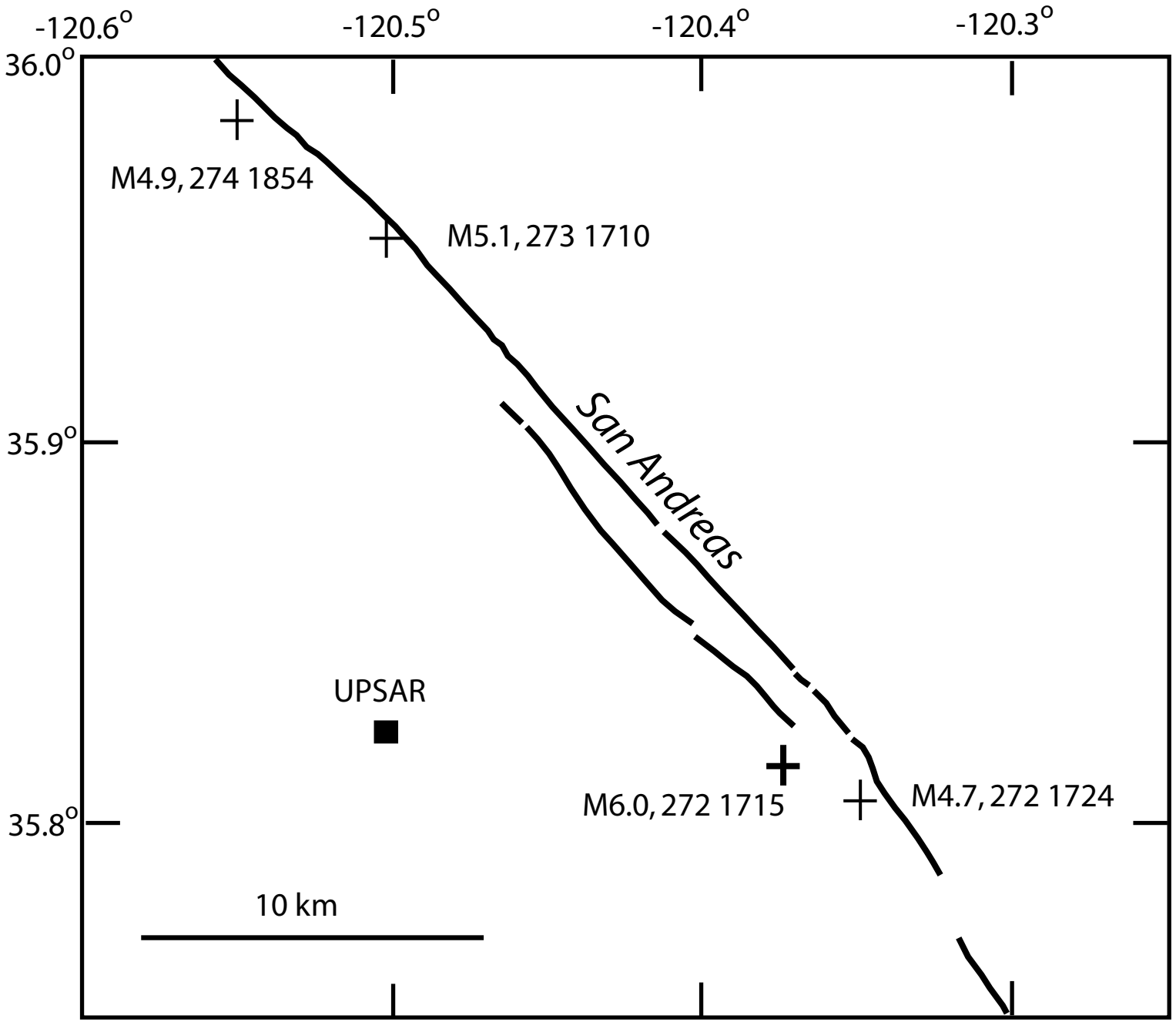
-120.6°
-120.5°
-120.4°
-120.3°
36.0°
35.9°
35.8°
M4.9, 274 1854
M5.1, 273 1710
San Andreas
UPSAR
M6.0, 272 1715
M4.7, 272 1724
10 km

Figure 2

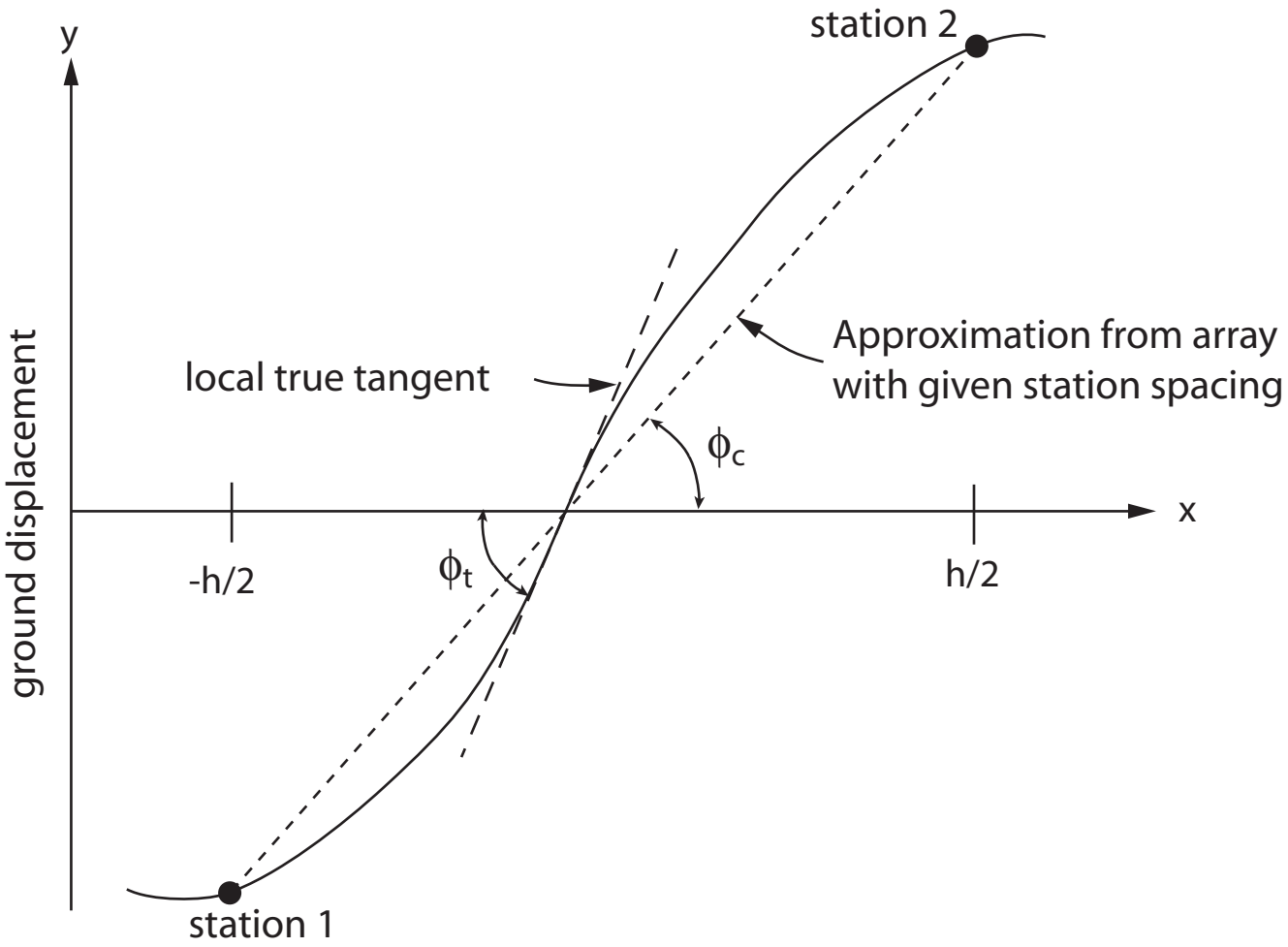
y
station 2
ground displacement
local true tangent
Approximation from array
with given station spacing
ϕ_c
x
-h/2
ϕ_t
h/2
station 1

Figure 3

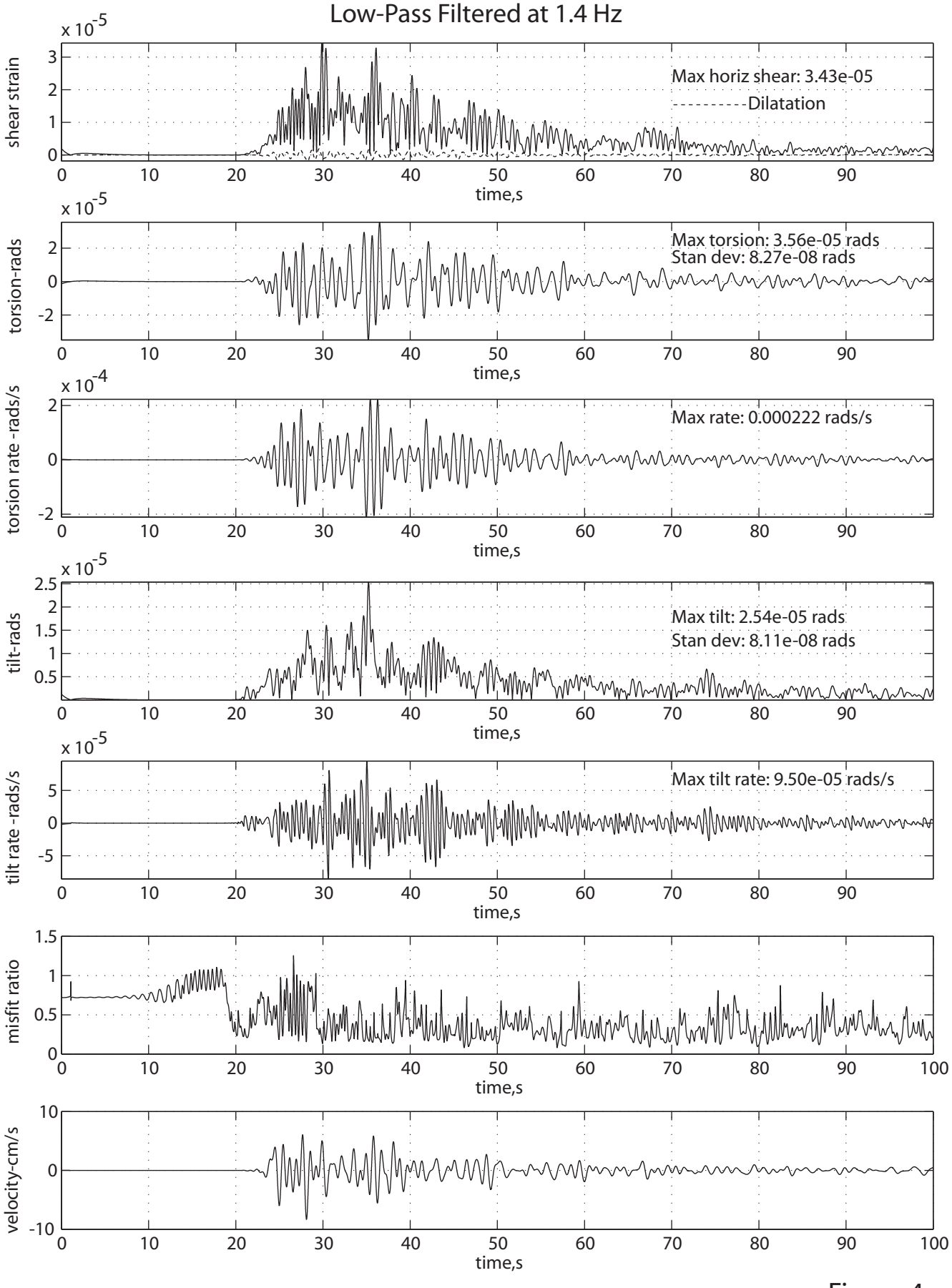
2004 Parkfield Mainshock M6.0 using Stations 5, 6, 7, 8, 9, 11, 12
Low-Pass Filtered at 1.4 Hz
shear strain
x 10^-5
Max horiz shear: 3.43e-05
Dilatation
torsion-rads
Max torsion: 3.56e-05 rads
Stan dev: 8.27e-08 rads
torsion rate -rads/s
x 10^-4
Max rate: 0.000222 rads/s
tilt-rads
Max tilt: 2.54e-05 rads
Stan dev: 8.11e-08 rads
tilt rate -rads/s
Max tilt rate: 9.50e-05 rads/s
misfit ratio
velocity-cm/s
time,s

Figure 4

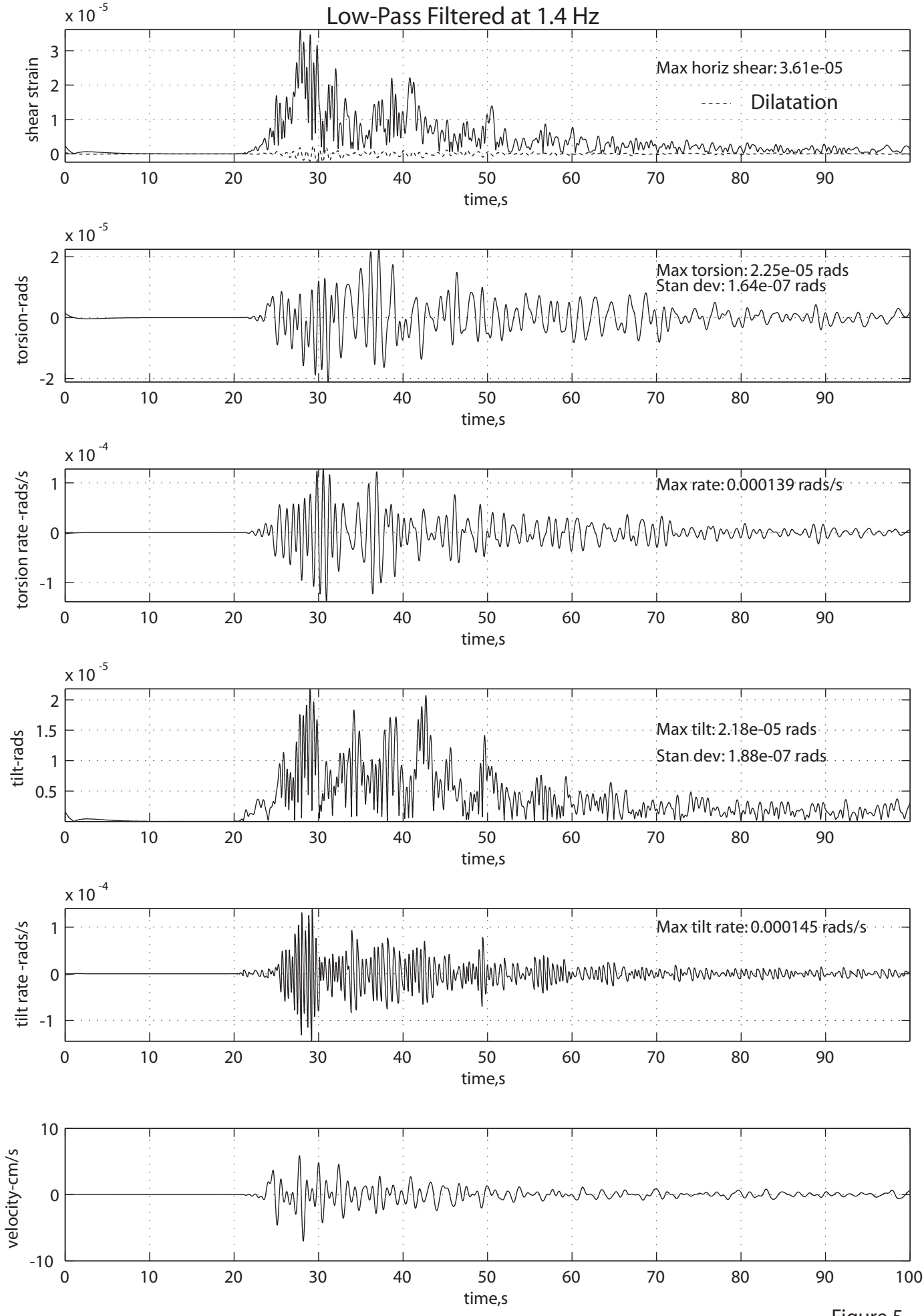
2004 Parkfield Mainshock M6.0 Using Stations 1, 2, and 3,
Low-Pass Filtered at 1.4 Hz
x 10 -5
shear strain
Max horiz shear: 3.61e-05
Dilatation
time,s
x 10 -5
torsion-rads
Max torsion: 2.25e-05 rads
Stan dev: 1.64e-07 rads
time,s
x 10 -4
torsion rate -rads/s
Max rate: 0.000139 rads/s
time,s
x 10 -5
tilt-rads
Max tilt: 2.18e-05 rads
Stan dev: 1.88e-07 rads
time,s
x 10 -4
tilt rate -rads/s
Max tilt rate: 0.000145 rads/s
time,s
velocity-cm/s
time,s

Figure 5

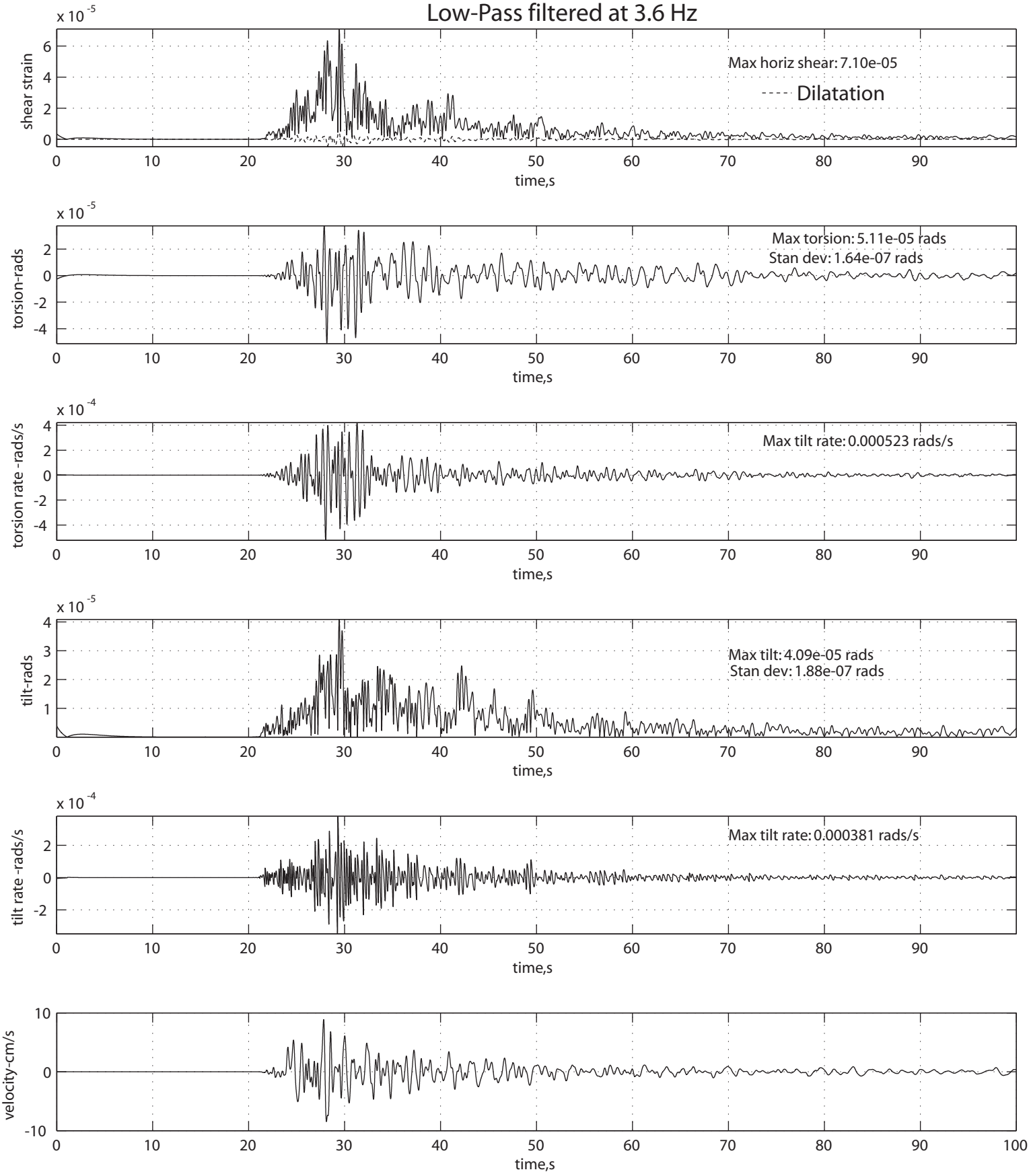
2004 Parkfield Mainshock M6.0 Using Stations 1, 2, and 3
Low-Pass filtered at 3.6 Hz
x 10 -5
shear strain
Max horiz shear: 7.10e-05
Dilatation
time,s
x 10 -5
torsion-rads
Max torsion: 5.11e-05 rads
Stan dev: 1.64e-07 rads
time,s
x 10 -4
torsion rate -rads/s
Max tilt rate: 0.000523 rads/s
time,s
x 10 -5
tilt-rads
Max tilt: 4.09e-05 rads
Stan dev: 1.88e-07 rads
time,s
x 10 -4
tilt rate -rads/s
Max tilt rate: 0.000381 rads/s
time,s
velocity-cm/s
time,s

Figure 6

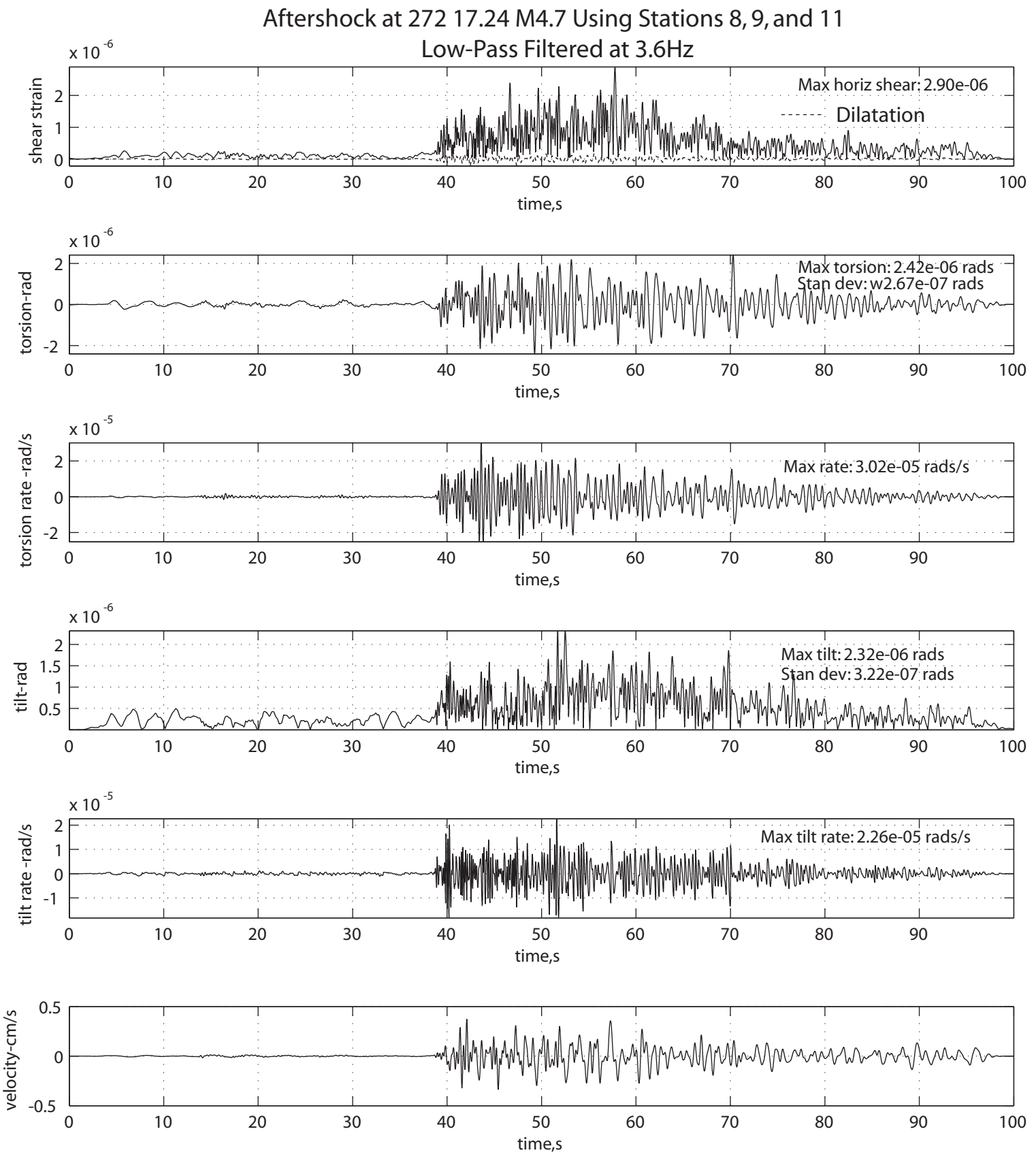
Aftershock at 272 17.24 M4.7 Using Stations 8, 9, and 11
Low-Pass Filtered at 3.6Hz
x 10 -6
shear strain
Max horiz shear: 2.90e-06
Dilatation
time,s
x 10 -6
torsion-rad
Max torsion: 2.42e-06 rads
Stan dev: w2.67e-07 rads
time,s
x 10 -5
torsion rate -rad/s
Max rate: 3.02e-05 rads/s
time,s
x 10 -6
tilt-rad
Max tilt: 2.32e-06 rads
Stan dev: 3.22e-07 rads
time,s
x 10 -5
tilt rate -rad/s
Max tilt rate: 2.26e-05 rads/s
time,s
velocity-cm/s
time,s

Figure 7

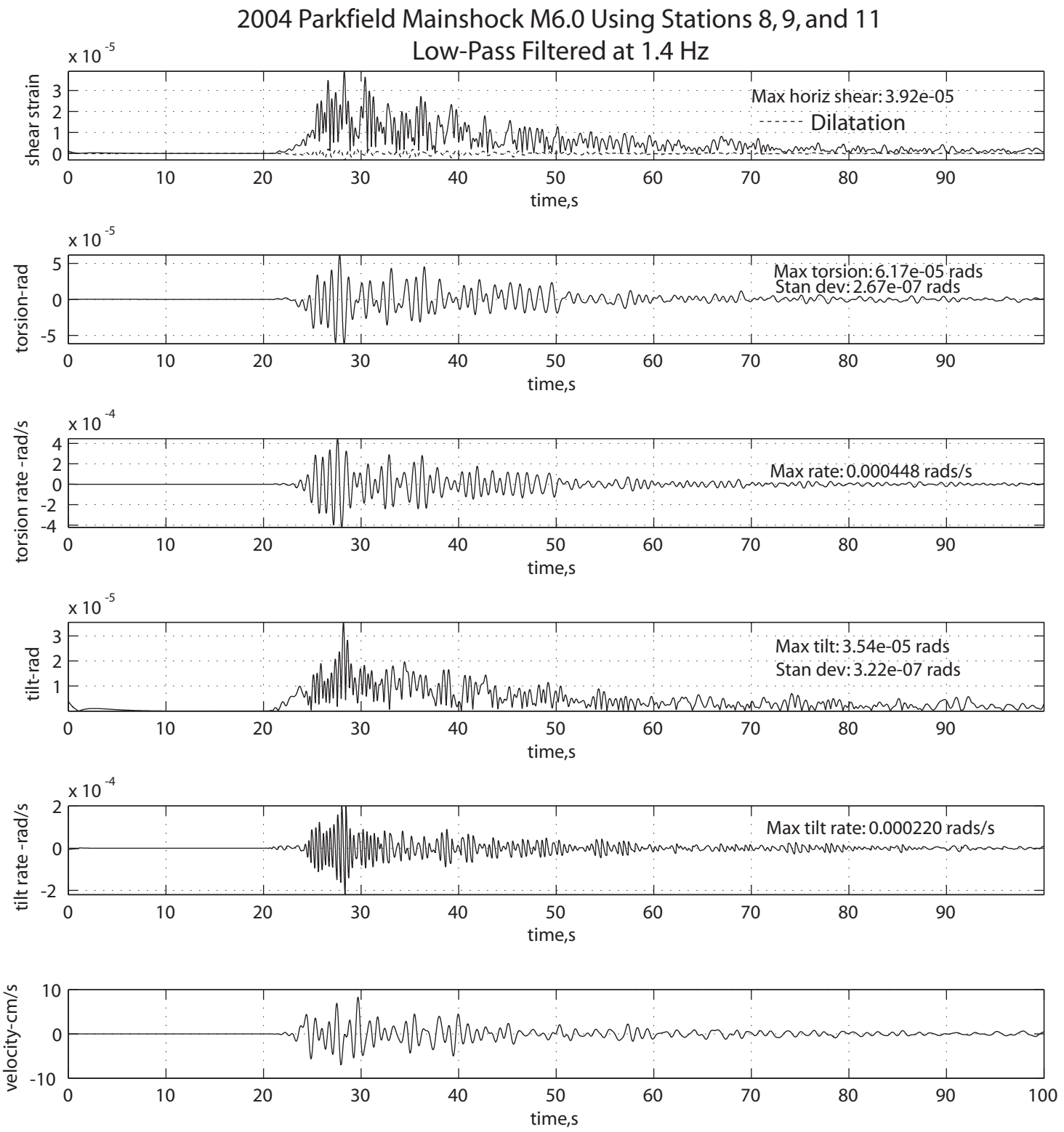
2004 Parkfield Mainshock M6.0 Using Stations 8, 9, and 11
Low-Pass Filtered at 1.4 Hz
x 10 -5
shear strain
Max horiz shear: 3.92e-05
Dilatation
time,s
x 10 -5
torsion-rad
Max torsion: 6.17e-05 rads
Stan dev: 2.67e-07 rads
time,s
x 10 -4
torsion rate -rad/s
Max rate: 0.000448 rads/s
time,s
x 10 -5
tilt-rad
Max tilt: 3.54e-05 rads
Stan dev: 3.22e-07 rads
time,s
x 10 -4
tilt rate -rad/s
Max tilt rate: 0.000220 rads/s
time,s
velocity-cm/s
time,s

Figure 8

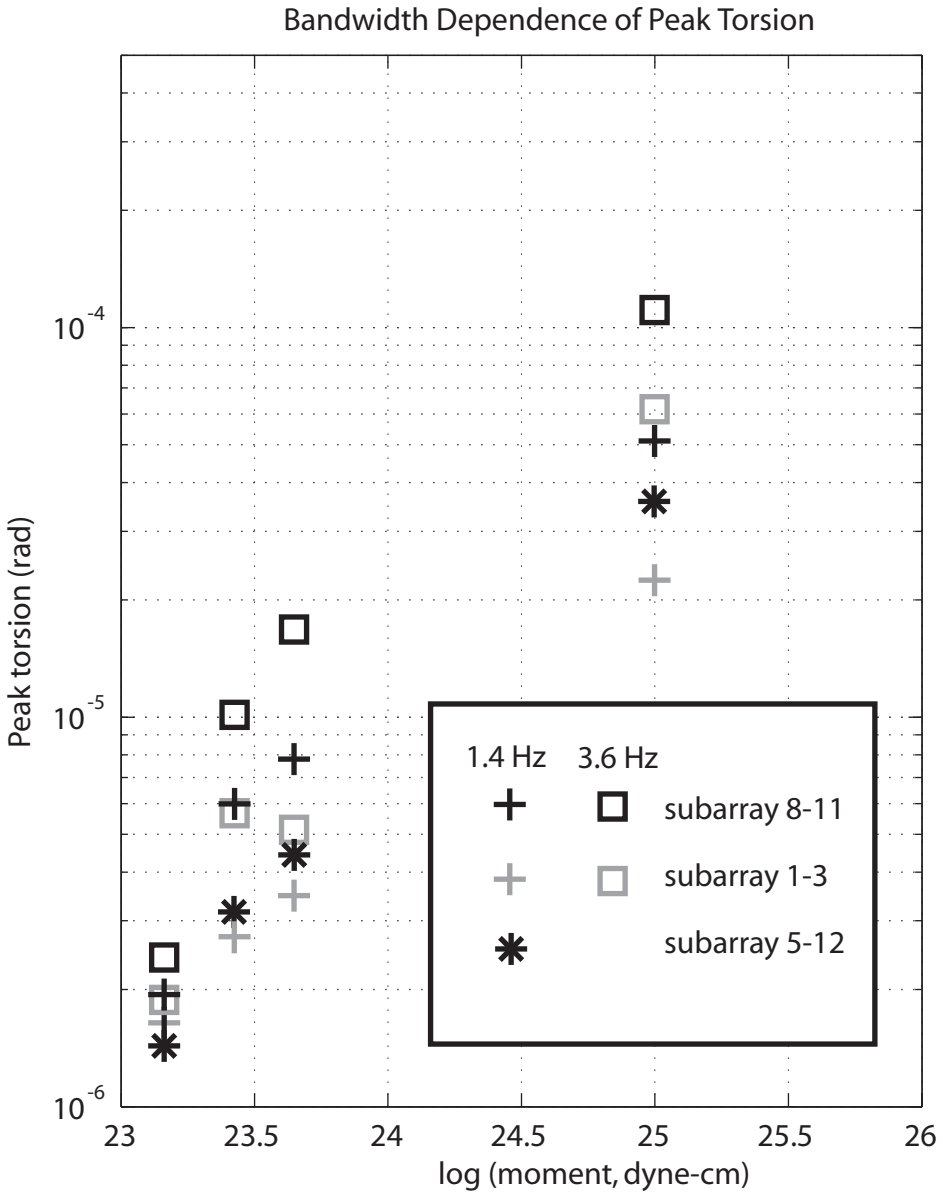
Bandwidth Dependence of Peak Torsion
Peak torsion (rad)
10^-4
10^-5
10^-6
23
23.5
24
24.5
25
25.5
26
log (moment, dyne-cm)
1.4 Hz
3.6 Hz
subarray 8-11
subarray 1-3
subarray 5-12

Figure 9

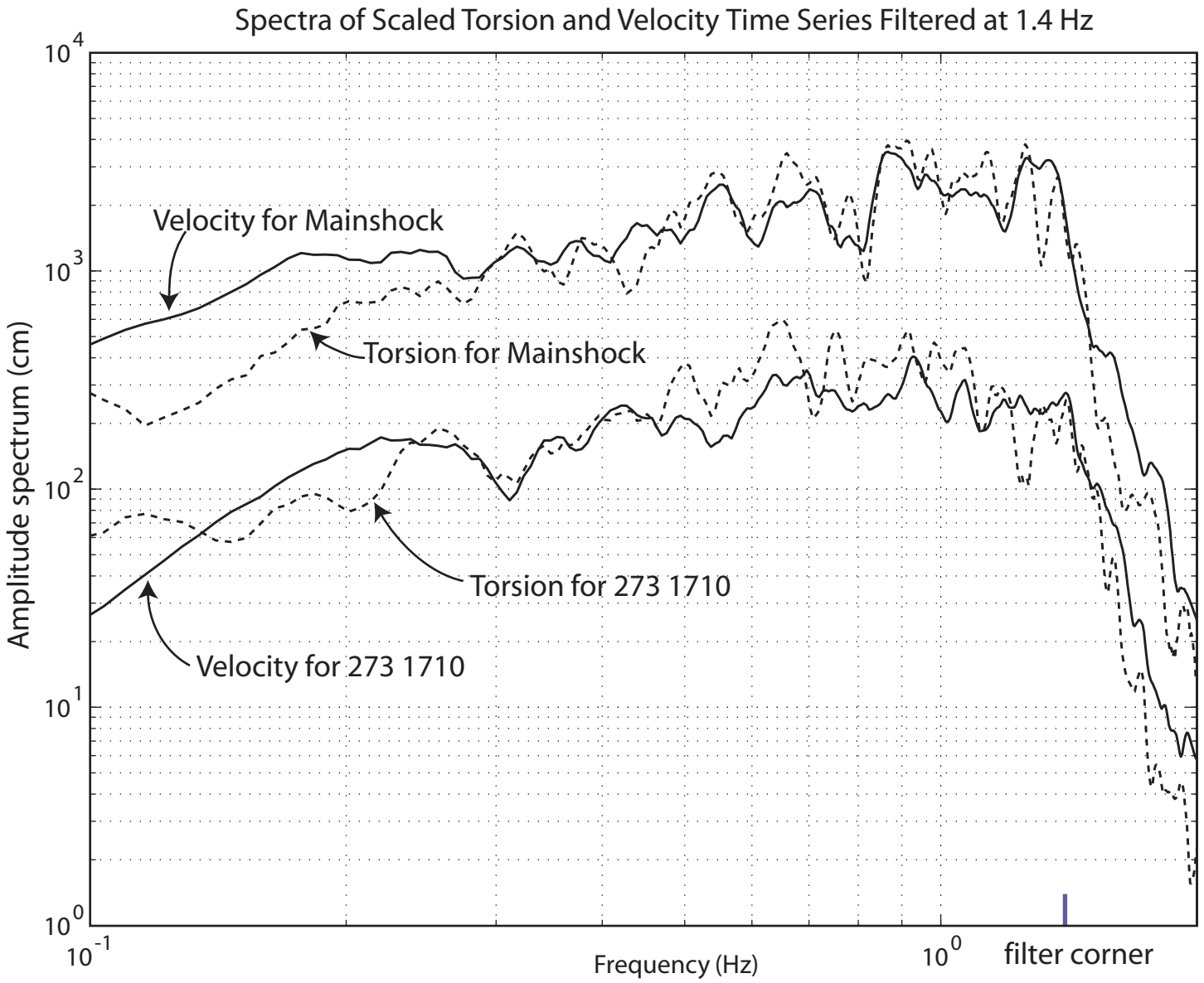
Spectra of Scaled Torsion and Velocity Time Series Filtered at 1.4 Hz
Amplitude spectrum (cm)
Frequency (Hz)
Velocity for Mainshock
Torsion for Mainshock
Torsion for 273 1710
Velocity for 273 1710
filter corner

Figure 10

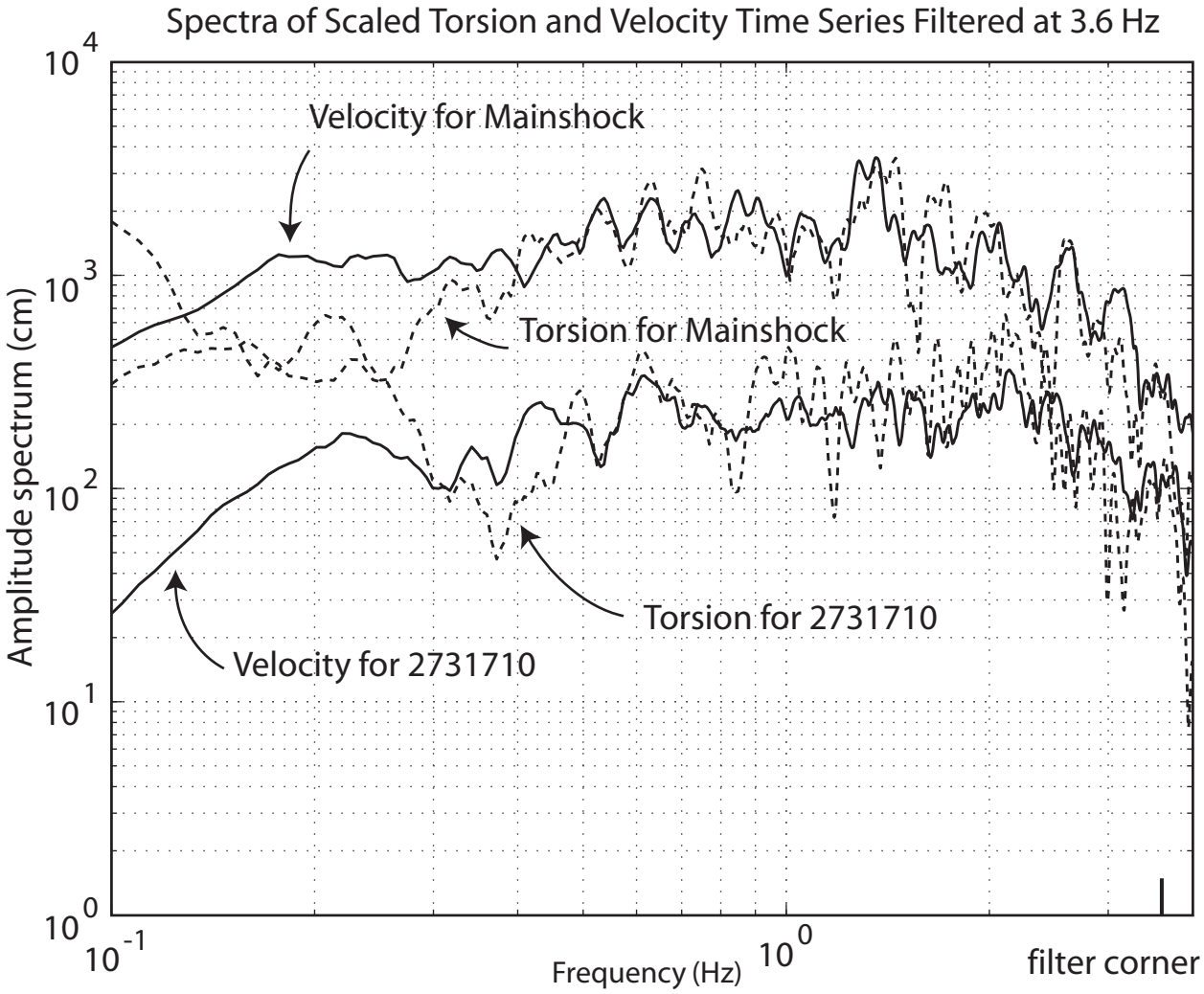
Spectra of Scaled Torsion and Velocity Time Series Filtered at 3.6 Hz
Velocity for Mainshock
Torsion for Mainshock
Torsion for 2731710
Velocity for 2731710
Amplitude spectrum (cm)
Frequency (Hz)
filter corner
10^4
10^3
10^2
10^1
10^0
10^-1
10^0

Figure 11

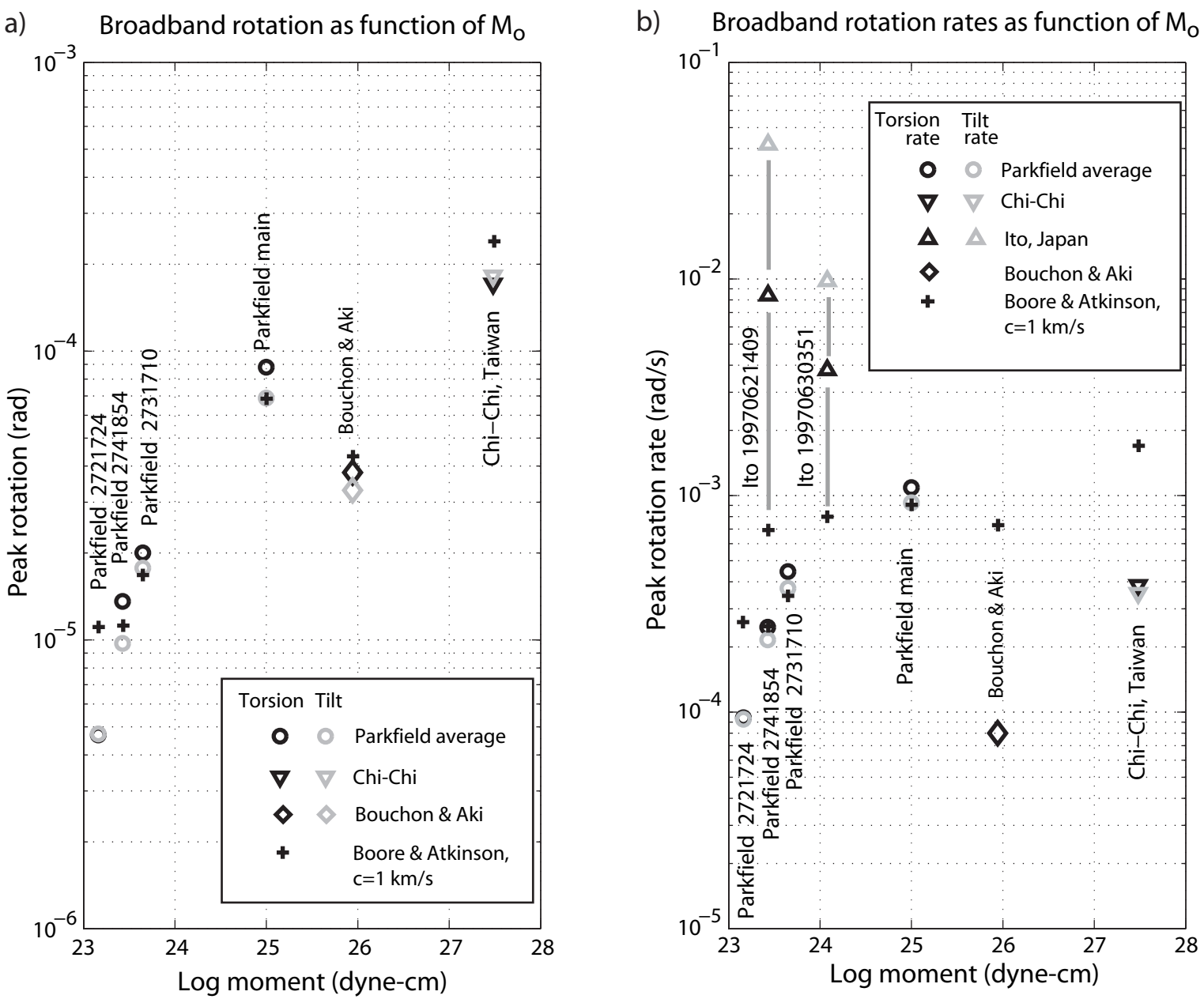
a)
Broadband rotation as function of M_o
Peak rotation (rad)
Log moment (dyne-cm)
Parkfield 2721724
Parkfield 2741854
Parkfield 2731710
Parkfield main
Bouchon & Aki
Chi–Chi, Taiwan
Torsion
Tilt
Parkfield average
Chi-Chi
Bouchon & Aki
Boore & Atkinson, c=1 km/s
b)
Broadband rotation rates as function of M_o
Peak rotation rate (rad/s)
Log moment (dyne-cm)
Ito 19970621409
Ito 19970630351
Torsion rate
Tilt rate
Parkfield average
Chi-Chi
Ito, Japan
Bouchon & Aki
Boore & Atkinson, c=1 km/s

Figure 12